DEM models using direct and indirect shape descriptions for Toyoura sand along monotonous loading paths

Tarek Mohamed, Jérôme Duriez, Guillaume Veylon, Laurent Peyras

DEM models using direct and indirect shape descriptions for Toyoura sand along monotonous loading paths

Tarek Mohamed, Jérôme Duriez, Guillaume Veylon, Laurent Peyras

DEM models using direct and indirect shape descriptions for Toyoura sand along monotonous loading paths

T. Mohamed[a], J. Duriez[a,*], G. Veylon[a], L. Peyras[a]

[a]*INRAE, Aix Marseille Univ, RECOVER, Aix-en-Provence, France*

Abstract

Two different DEM models are proposed for quantitatively simulating Toyoura sand macroscopic response along various monotonous loading paths and for a wide range of initial densities. The first model adopts spherical particles and compensates for the irregular shapes of Toyoura sand grains by adding an additional rolling resistance stiffness to the classical linear contact model. The second model follows a different strategy whereby rolling stiffness is abandoned in favor of more complex shapes in the form of a few different 3D polyhedrons defined from a 2D micrograph of Toyoura particles. After a preliminary analysis of the number of particles for optimal REV simulations, the two different modeling approaches are calibrated using triaxial compression in so-called drained conditions, adopting a common contact friction angle for the two models. Similar predictive abilities are then obtained along so-called undrained (constant volume) triaxial compression and extension paths. Although it leads to 9-times longer simulations, the polyhedral approach is easier to calibrate regarding the contact parameters. It also enables a more precise description of the microstructure in terms of particle shapes and initial fabric anisotropy, whose crucial role is evidenced in a parametric analysis.

Keywords: Toyoura sand, DEM, Rolling resistance contact model, Polyhedral particles, Anisotropy

*Corresponding author
Email address: `jerome.duriez@inrae.fr` (J. Duriez)

1. Introduction

As a discrete material, sand exhibits a complex behavior when subjected to external loading, showing material anisotropy, non-linear stress-strain response, contraction or dilation depending on the void ratio, and additional plastic strain on a loading-unloading path. That mechanical behavior depends on interparticle friction and on possible loss or gain of contacts between grains when sand is exposed to an anisotropic or isotropic loading. While materials are most often subjected to anisotropic loadings in a realistic setting, this leads to an anisotropic evolution of the contact normal fabric tensor (Oda et al., 1985), whereby normal vectors tend to align progressively in the direction of the loading applied until a constant direction is reached at the critical state (Li and Dafalias, 2012). Since the Discrete Element Method (DEM) (Cundall and Strack, 1979) tracks the dynamic motion of each individual particle defined in terms of mass, shape, and inertia, it reproduces directly these discrete phenomena and can be used as a powerful alternative technique to classical soil constitutive models (Nguyen et al., 2014). Indeed, relevant macro-scale solid behaviors have been obtained both qualitatively by e.g. Wang et al. (2016); Yimsiri and Soga (2010) and quantitatively by Hosn et al. (2017); Lee et al. (2012); Gu et al. (2020); Rorato et al. (2021) on different sands.

For the sake of simplicity, classical 3D-DEM simulations use spherical shaped particles to represent the grains of granular materials, however, the real shapes of grains are irregular and far from being that simple. For example, Miura et al. (1998) presented the substantial influence of grain shape on the stress-strain response of sands. Furthermore, studies on angular stainless steel powder (Shinohara et al., 2000) highlighted the direct relation between particle angularity and particle interlocking. Numerically, attempts have been made to represent grain shapes inside DEM simulations starting with an additional rotational spring at the contact level (Iwashita and Oda, 1998; Jiang et al., 2015; Irazábal et al., 2017; Hosn et al., 2017; Ai et al., 2011; Sibille et al., 2019; Gu et al., 2020; Rorato et al., 2021) so that it can resist relative rotation and indirectly introduce the effect of the particle shapes on the DEM simulations to some extent. On the other hand, clumping/overlapping a number of spheres enables one to directly approximate shapes of real particles e.g. (Garcia et al., 2009; Katagiri et al., 2010; Sibille et al., 2019), though with a possible negative effect of the excessive roundness value for clumps on the material response. A third strategy is to introduce convex polyhedral shapes inside the DEM simulation (Lee et al., 2012; Nassauer et al., 2013). This strategy may seem to be more realistic since the morphology of the grains can be reproduced correctly and computational time can be optimized with an adequate number of vertices. In the case where a higher number of vertices may be required, it seems interesting to eventually resort to a level set strategy (Jerves et al., 2016; Duriez and Bonelli, 2021) whereby a distance-to-surface function is considered, in a discrete fashion, for every grain and contact is detected through a simple interrogation of these distance data.

In the particular case of Toyoura sand chosen as a quite standard material for geomechanics, previous DEM approaches have adopted both spherical particles in conjunction with rolling resistance (Gu et al., 2020) and clump strategies (Katagiri et al., 2010) for quantitative comparisons with experiments. While the inclusion of clumps was somewhat beneficial, there were still some difficulties in both studies for obtaining quantitative DEM results that could closely fit different experiments on Toyoura sand with very different initial void ratios.

The present analysis aims to extend the knowledge corpus on Toyoura sand and these previous DEM studies, proposing efficient and versatile DEM approaches for a discrete-based, quantitative simulation of that material. More specifically, two 3D-DEM models are developed to simulate the mechanical behavior of Toyoura sand in porosity and loading conditions yet unexplored from a quantitative point of view. The first model is a spherical grain model that incorporates rolling resistance. A second model aims to directly introduce realistic shapes of Toyoura sand grains by using convex polyhedral particles. Section 2 describes the DEM formulations and the setup of the polyhedral and sphere models while using PFC 6 software (Itasca, 2018). Section 3 presents a parametric study and calibration procedures for the two models including a brief study on a proper REV definition, for an optimal setup of the 3D-DEM models. Finally, Section 4 shows the validation of the two models along various stress paths (drained and undrained triaxial compression and extension) and different initial void ratio values.

2. DEM formulations

2.1. Contact detection and resolution

Every DEM cycle, contact detection and resolution schemes are applied prior to the application of a constitutive contact relation. The contact detection process starts with a broad phase where an axis-aligned bounding box (extended cell) is generated for each particle. Contact is possible once two extended cells of two pieces overlap. The second step includes a narrow phase contact detection algorithm by which the pair of pieces identified as possibly colliding objects will be investigated in more detail. In the case of spheres interactions, the process is straightforward since it is sufficient to detect the contact by knowing the position of the spheres and their radii.

However, in the case of polyhedrons, the process is much more complicated and the Gilbert-Johnson-Keerthi (GJK) algorithm (Gilbert et al., 1988) is executed in PFC. The latter is an efficient iterative algorithm used to detect the overlapping state between two convex objects. It is based on the concept of the Minkowski difference of two convex polyhedrons, i.e. a convex polyhedron itself which includes the origin if the two bodies overlap, while working in an iterative simplex-algorithm manner to possibly avoid a full computation of that difference. In order to further save computational time, the GJK algorithm is applied in PFC while considering that a particle shape actually includes a core polyhedron which is extended by sweeping spheres, whose common diameter is given by a rounding coefficient also discussed in Section 3.2. Particles interaction is then obtained as soon as the Minkowski difference of core polygons approaches the space origin within the margin of the rounding coefficient, see

Figure 1. The same approach can for instance be found in contact algorithms proposed by Zhao and Zhao (2021) for superellipsoids.

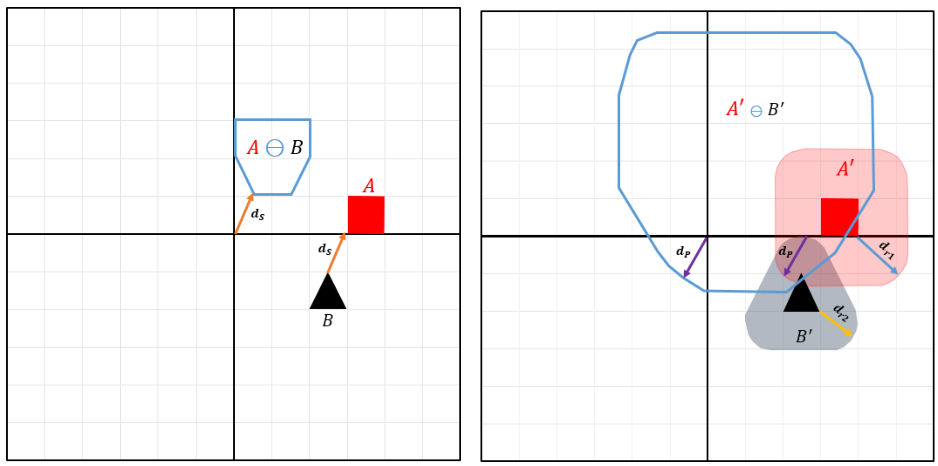

Figure 1: Contact detection and Minkowski difference for two convex particles A and B, whose core polygons do not overlap (Left) but that are still in contact due to rounding (Right, rounding artificially enlarged): 2D illustration for clarity.

Denoting $d_s > 0$ the separation length between the two core shapes as obtained from the Minkowski difference, $d_{r1} > 0$ and $d_{r2} > 0$ the rounding values of the two particles, a penetration depth $d_p \leqslant 0$ can be obtained for contacting particles as follows:

$$d_p = d_s - d_{r1} - d_{r2} \tag{1}$$

Contact normal is also obtained from that construction of d_p (Figure 1), while contact location is finally defined as the center of the overlapped area and determined based on other algorithms (Preparata and Muller, 1979; Shamos and Hoey, 1976).

That GJK-based determination of contact normal and penetration depth may fail depending on relative positions and rounding coefficient. In this case, the Expanding Polytope Algorithm (EPA, Bergen, 1999) is applied by PFC, with a higher computational demand.

In both cases, this contact resolution scheme logically affects computational times depending on the number of polyhedra vertices and those costs will be estimated in Section 4.2.

2.2. Inter-particle contact models

Interacting particles first sustain contact forces following a classical linear contact model. An elastic normal contact force first evolves as follows:

$$\vec{f_n} = K_n \vec{\delta}_n \tag{2}$$

$$K_n = E_{mod} \frac{\pi r^2}{R_1 + R_2} \ with \ r = min(R_1, R_2) \tag{3}$$

where $\vec{\delta}_n$ is the relative normal-displacement along the contact normal $\vec{n}_c$ and K_n is the normal stiffness function of the normalized parameter E_{mod} and of R_1 and R_2 the radii of the two contacting spheres. The linear shear force is updated incrementally as follows:

$$\vec{f_s} = \vec{f_s^0} + K_s \Delta \vec{\delta}_s \tag{4}$$

where $\vec{f_s^0}$ is the linear shear force at the beginning of a time step and K_s the contact tangential stiffness. The source of the shear displacement $\vec{\delta}_s$ is the relative tangential velocity at the contact point including the linear and angular relative velocities of the bodies. Finally, the Coulomb friction condition is imposed to limit the shear force of the contact as follows:

$$||\vec{f_s}|| \leqslant ||\vec{f_n}||\mu \tag{5}$$

where μ is the friction coefficient. This contact model applies to both proposed models (sphere and polyhedron).

In addition, a rolling resistance stiffness is also incorporated at the contact level inside the sphere model in order to compensate for the non-sphericity of the real sand particles. The contact moment is incremented linearly with the accumulated relative rotation of the contacting pieces. At the contact level the rolling stiffness and moment incremental laws are characterized as follows:

$$K_r = K_s R_m^2 \tag{6}$$

$$\frac{1}{R_m} = \frac{1}{R_1} + \frac{1}{R_2} \tag{7}$$

$$\Delta\vec{M}_r = K_r \Delta\vec{\theta}_b \quad ||\vec{M}_r|| \leqslant \mu_r ||\vec{f}_n|| R_m \tag{8}$$

$$\Delta\vec{\theta}_b = \Delta\vec{\theta} - \Delta\theta_t . \vec{n}_c \tag{9}$$

Where μ_r, R_m, $\Delta\vec{\theta}$ and $\Delta\vec{\theta}_b$ are defined as the rolling friction coefficient, effective radius, rotation increment and relative bend-rotation increment, respectively. Equation 9 shows that for the present contact law, the twisting rotational component $\Delta\theta_t$ does not contribute to the rotational increment that is used in the rolling friction law.

2.3. A 2D-image-based 3D polyhedral description of Toyoura sand grains

When introducing the real grain shapes directly into DEM simulations, convex polyhedrons are used as 3D elements which consist of a number of vertices forming triangle facets. While the convexity of particles is an inherent limitation of the approach and PFC software, it will be checked it has no detrimental consequences on the results since Toyoura sand grains are measured to be close to convex by Liu and Yang (2018), with a 2D convexity = 0.937 in average while unit values would correspond to truly convex particles.

The definition of the present 3D polyhedral elements for Toyoura sand relies on a very simple 2D image-based workflow where a microscopic photograph of Toyoura sand is used (Fig. 2) to build three representative shapes of Toyoura sand grains, instead of the spherical grains. According to Fig. 2, Toyoura sand particles have a wide variety of shapes and different aspect-ratio values that range at least from 1.5 to 2.3, consistent with computed tomography data presented by Katagiri et al. (2010). From these observations, we propose to create just three polyhedral shapes that may reflect these morphological traits.

The preparation procedure is relatively simple starting from 3D PFC templates of convex polyhedrons and then trying to manually adapt the vertices positions to fit and mimic the form of the 2D-image of Toyoura sand. The aspect ratio is used to assess how close the proposed shapes are to the real grains. It is uniquely defined as the ratio between the largest and the middle principal dimensions: L_1/L_2 denoting $L_3 \leqslant L_2 \leqslant L_1$ the three principal dimensions of particles. In the case of the 2D image, the information about the third (smallest) principal direction L_3 is logically missing and it is arbitrarily assumed as $L_3 = 0.75\, L_2$ for the three convex polyhedrons. While there is no a prior justification for this assumption, the subsequent successful calibration and validation of the model will confirm its usefulness. In addition, the roundness of these three shapes is minimized since Toyoura sand is characterized by its sharp edges. The effect of roundness and aspect ratio on the DEM simulations will be investigated in more detail in section 3.2. Finally, the three convex polyhedrons created present different aspects and in the same time fit within the lower, middle, and upper ranges of the aspect-ratio values of Toyoura sand, as shown in Fig. 2. Indeed, Table 1 shows a high convergence between the aspect-ratio values for the proposed shapes (forming a default “Group 1”) and the real particles. An auxiliary ”Group 2” of 3 shapes is also proposed after reducing each aspect ratio i.e. the length of the larger principal dimension L_1 while keeping the length of the two other principal dimensions constant, for the purpose of a parametric analysis in Section 3.

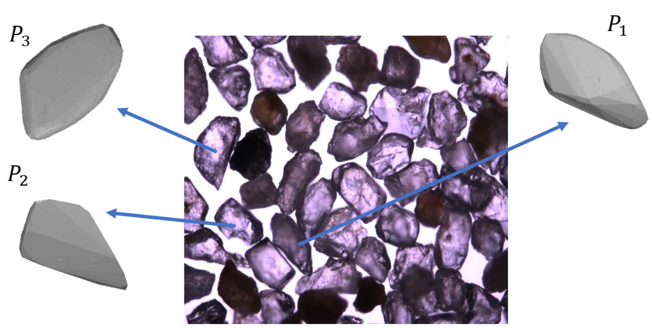

Figure 2: Original micrograph of the particle shape of Toyoura sand (Li, 2011) vs the three proposed shapes (Group 1).

Finally, the true sphericity shape parameter (Wadell, 1932) is also used to

Table 1: 3D-DEM polyhedra aspect-ratio vs Toyoura sand aspect-ratio

Toyoura Particle	2D-image from Fig. 2	3D-DEM Group 1	3D-DEM Group 2, see § 3.2
P_1	2.3	2.3	1.6
P_2	1.59	1.59	1.1
P_3	1.86	1.85	1.3

assess the shape definition of the 3D convex polyhedrons. The true sphericity parameter is defined as follows:

$$\psi = \frac{S_{Sphere}}{S_{Polyhedron}} \tag{10}$$

Where S_{Sphere} is the surface area of a sphere of the same volume as the particle and $S_{Polyhedron}$ is the actual surface area of the particle. Fig. 3 presents the values of the true sphericity of each particle. True sphericity values are consistent with those presented by Rorato et al. (2021) from computed tomography on Hostun sand, which shares a similar angularity with Toyoura sand (Altuhafi et al., 2013). Also, Fig. 3 shows that the true sphericity values of Group 1 are lower than the values of Group 2 which are aligned with the higher aspect ratio values of Group 1.

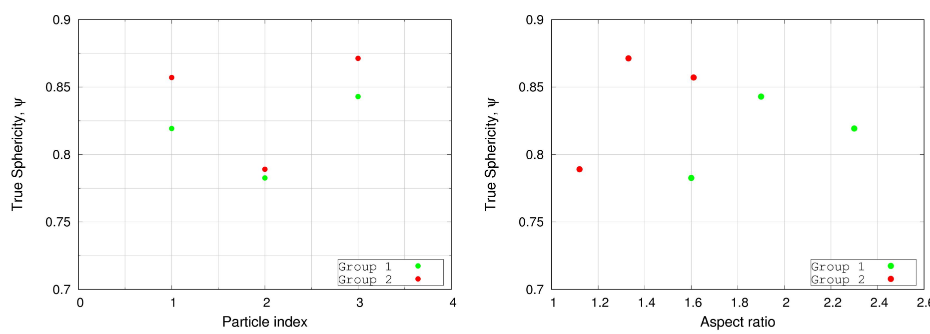

Figure 3: Left: true sphericity values of the different particles in Group 1 and Group 2. Right: Aspect ratio values vs true sphericity values for Group 1 and Group 2.

Finally, Table 2 presents the number of facets and vertices for each particle, as directly obtained after manually adapting the templates and retaining their convex hulls for the PFC computations. In addition to computational time, the obtained mechanical behavior also depends on that resolution in the shape description. A systematic study on that aspect is nevertheless outside the present scope, while the model results will serve as the sole justification for these properties.

Table 2: 3D-DEM polyhedra particles number of vertices and facets for Group 1

Particle	Number of vertices	Number of facets
P_1	128	252
P_2	78	152
P_3	203	402

2.4. Numerical packing and generation procedure

For spheres, the same particle size distribution as Toyoura sand is used in these simulations as shown in Fig. 4, modulo a scaling factor which is mechanically transparent by virtue of the contact model, e.g. Eq. 3. Regarding the 3D-DEM polyhedral model, the ratio between the maximum and minimum convex polyhedron size is assigned for simplicity to be the same as the uniformity coefficient C_U of Toyoura sand and equal to 1.7, as shown in Fig. 4. Size is defined for the polyhedrons based on the sphere being equivalent in volume. The three representative shapes inside the generated sample share the same number of particles. Note that the present 3D-DEM approaches do not consider the particle-crushing phenomenon which would exist at high pressures (Yokura et al., 2015), while the present simulations are performed for relatively low-pressure cases (maximum confining pressure is 400 kPa).

Particles are enclosed within a rectangular parallelepiped with initial dimensions of L_X=200 mm, L_Y=200 mm, L_Z=300 mm and the sample is stressed using rigid walls. Unless otherwise specified, numerical samples contain around 7500 particles as shown in Fig. 5 and justified in next Section 2.5.

The DEM microstructure is assessed by examining both the evolution of the contact normal fabric tensor and the evolution of the coordination number during the different tests. The coordination number of an assembly of particles

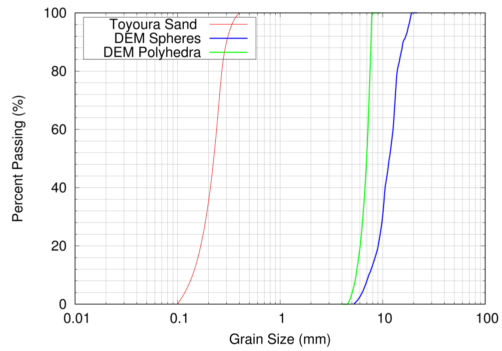

Figure 4: Particle size distributions of Toyoura sand (after Dong et al., 2016) vs DEM models.

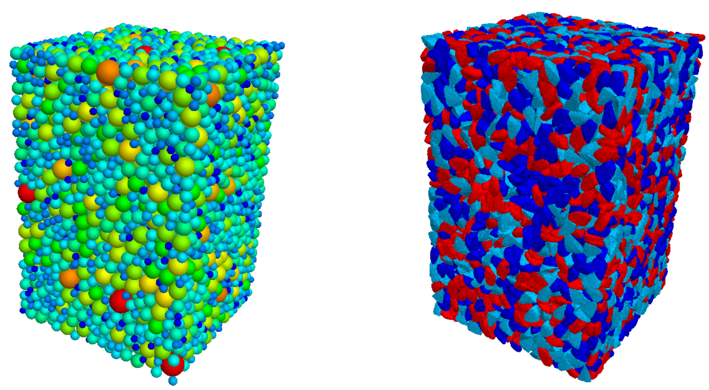

Figure 5: The two 3D-DEM models with different particle shapes: left spherical particles, where colors correspond to diameters; right convex polyhedral, where different colors correspond to different shapes (particles P_1,P_2,P_3).

can be expressed as follows:

$$Z = \frac{2N_c}{N_b} \tag{11}$$

where N_c is the number of contacts and N_b is the number of bodies. The contact normal fabric tensor F_{ij} can be evaluated as follows:

$$F_{ij} = \frac{1}{N_c} \sum_{cont.} n_i \otimes n_j \tag{12}$$

where n_i is the contact normal direction. The anisotropy A of the fabric tensor F_{ij} is quantified and defined as the ratio between the deviatoric part of the fabric tensor and one-third of the first invariant of the fabric tensor. By taking into account the axisymmetric condition of the triaxial test around axis Z, the equation yields to:

$$A = \frac{3(F_{ZZ} - F_{XX})}{F_{ZZ} + 2F_{XX}} = 3(F_{ZZ} - F_{XX}) \Rightarrow |A| = 3(F_I - F_{III}) \tag{13}$$

Where F_I and $F_{III} = F_{II}$ are the fabric eigenvalues.

Inspired by laboratory tests where samples could be prepared by using different methods such as air pluviation (Tatsuoka et al., 1986) or moist tamping (Verdugo and Ishihara, 1996) with an influence on initial fabric, two different procedures are herein adopted for packing generation.

As a first option, DEM samples are prepared starting from a cloud of particles with no contacts. Afterwards, an isotropic compaction is applied by moving the walls towards the sample with maximum velocity and target compaction pressure. During the compaction phase, porosity can be controlled depending on the friction coefficient and rolling coefficient (for the spherical cases) values which are tuned, independently of the subsequent shear loading phase, to reach the same initial porosity values as the reference experiments considered below.

In a second preparation method, the cloud of non-overlapping particles is first let to settle under vertical acceleration (enhanced gravity). A top wall then moves downwards to ensure good contact with the particles before applying an isotropic pressure by moving the six walls towards the sample, until forming the consolidated stage of the triaxial loading.

The spherical model is observed to be insensitive to the preparation procedure for what concerns its fabric, which can be explained by the isotropic nature of spherical shapes, presented simulations with spheres then apply indistinctly to either preparation method and start with a fairly isotropic fabric. On the other hand, the polyhedron model shows a strong sensitivity to the preparation method, which will be discussed in connection with contact parameters in Section 3.3.

Finally, the quasi-static condition is ensured for the different triaxial tests by satisfying the following condition for the inertial number $I_r \leqslant 10^{-4}$.

2.5. Effect of the number of particles on 3D REV response

Because the DEM results are here classically interpreted in average through the consideration of stresses, strains or fabric tensor defined at the sample scale, it is important to check whether a Representative Elementary Volume (REV) is reached in the sense that the mechanical response is fully defined from the average initial properties (e.g. porosity) with no other influences coming e.g. from the placements of individual particles in each case. For given average initial properties, a previous study (Chareyre, 2003) illustrated how results dispersion (e.g. on peak values or volumetric response) possibly exists but decreases when the number of particles increases towards forming a REV. Previous 3D-DEM studies at the REV scale can be found with various numbers of particles, possibly as different as 1000 (Cheng et al., 2018) and about 44000 (Gu et al., 2020). A REV determination is then proposed in this study for the spherical model, investigating the effect of the number of particles on the homogeneity of the REV and its impact on the computational time, while keeping all the other parameters of the DEM simulation constant (Table 3). The number N of spheres in the sample is changed gradually from 400 to 14500 spheres, using smaller spheres and a constant total size of the sample since the present DEM results are particle size-independent.

To obtain a view inside the different samples, the porosity was monitored in two different ways. A first measure calculated the overall porosity n_b based on

Table 3: Spherical DEM parameters

Remark	Contact				Packing (see also Fig. 4 for psd)		
	E_{mod} (MPa)	K_n/K_s (-)	μ (-)	μ_r (-)	N_b (-)	Initial n_b (-)	Initial A (-)
REV analysis of Section 2.5	450	3	0.6	0.38	from 400 to 14500	0.402	0
Rolling resistance analysis of Section 3.1	450	3	0.6	0 or 0.38	7530	0.400	0
Proposed model for Toyoura sand (Sections 3.4 and 4)	450	3	0.6	0.38	7530	from 0.40 to 0.453	0

Eq. 14, representing the average porosity for the whole sample.

$$n_b = 1 - \frac{1}{L_x L_y L_z} \sum_{N_b} V_b \tag{14}$$

where N_b is the total number of (spherical) particles inside the sample and V_b is the volume of one ball. A second value of the porosity n_c is more local, being defined within a measurement region, as described in Eq. 15.

$$n_c = 1 - \frac{\sum_{Nb} V_b + \sum_{N_i} V_i - \sum_{b_c} V_c}{V_{reg}} \tag{15}$$

where V_i is the intersected volume between balls and the measurement region, N_i is the number of balls that intersect the measurement region and V_c is the overlapped volume between the balls that lie inside the measurement region. Here, the measurement region is a ball positioned at the center of the sample and has a diameter equal to 90 % of the shortest length of the sample. Thus, the homogeneity of the sample in terms of porosity can be evaluated by comparing the two calculated porosities mentioned previously.

Doing so, global porosity n_b is controlled to be equal to 0.402 for 9 samples with different numbers of particles, while the second value of the porosity n_c is locally evaluated for each sample. The results illustrated in Fig. 6 show that by increasing the number of particles, the sample becomes more homogeneous thanks to a smaller proportion of particles along boundaries and the values of the two calculated porosities become closer. On the other hand, for the samples that use lower numbers of particles, voids are concentrated at the volume that is adjacent to the peripheral walls. Fig. 6 also shows how computational time increases by increasing the number of particles used in the simulation. Computational times refer to a parallel execution of PFC on a workstation with 8 cores, 3.0 GHz CPU with 64 GB RAM. Finally, Fig. 7 shows that the effect of the number of particles on the deviatoric and volumetric responses becomes negligible starting from a number of particles N equal to 7500, defining the REV scale consistently with e.g. Duverger et al. (2021) on another granular material.

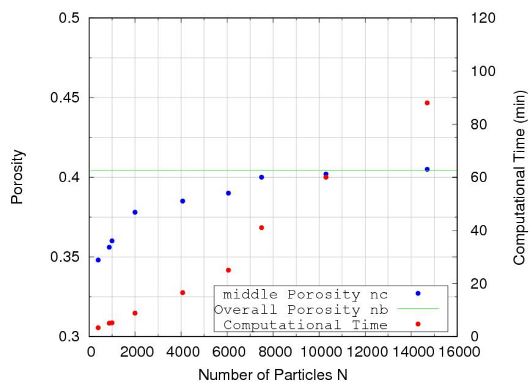

Figure 6: Number of spheres N vs computational time and n_c,n_b.

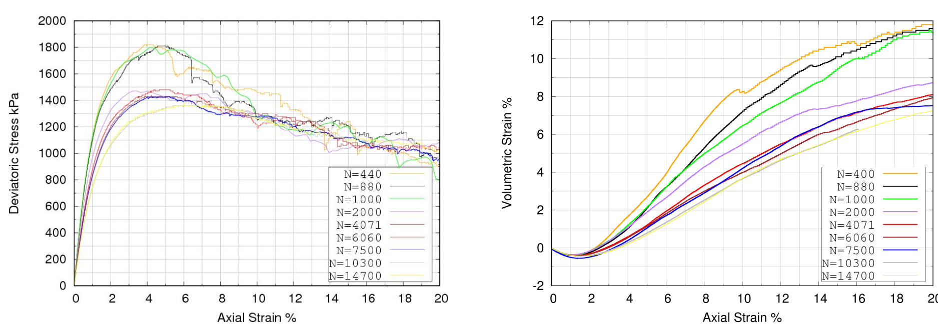

Figure 7: Effect of the number of particles on the deviatoric and volumetric responses for the same initial porosity n_b=0.402 and confining pressure = 400kPa.

3. Parametric analysis and calibration of the spheres and polyhedron models

An extended parametric study was performed on the sphere and polyhedron models. Concerning the sphere model, the study contained the effect of the presence or absence of the rolling resistance stiffness, see Table 3. For the polyhedron model, the study involved the effect of the shape parameters: aspect ratio or true sphericity, roundness, as well as the effect of the initial anisotropy value in conjunction with contact parameters. Table 4 presents a summary of the proposed simulations for the polyhedron model.

Table 4: Summary of simulations with the 3D-DEM polyhedron model

Object	Set number (from Table 5)	Polyhedrons Group (from Table 1)	Variable condition(s)
Influence of shape parameters in Section 3.2	Set 1	Group 1	Particles relative rounding [0.0001,0.01,0,5]
Influence of shape parameters in Section 3.2	Set 1	Group 1 vs Group 2	Particles aspect ratio (i.e. true sphericity)
Interplay of initial fabric with contact parameters in Section 3.3	Set 1 vs Set 2	Group 1	Sample preparation (i.e. initial fabric A) and contact parameters
Proposed model for Toyoura sand in Sections 3.4 and 4.1	Set 2	Group 1	Void ratios, confining pressures and loading paths

3.1. Influence of rolling resistance on the sphere model

The effect of the rolling resistance coefficient μ_r is investigated herein. Fig. 8 shows the results of DEM simulations with and without μ_r together with the corresponding experimental data for a drained triaxial test for Toyoura sand obtained by Fukushima and Tatsuoka (1984). Fig. 8 shows the advantage that can be added by the rolling resistance friction law to the strength and volumetric strain behaviors for the sphere model. In addition, the simulations confirm the crucial role played by the rolling stiffness to represent the irregular-shaped particles of Toyoura sand indirectly.

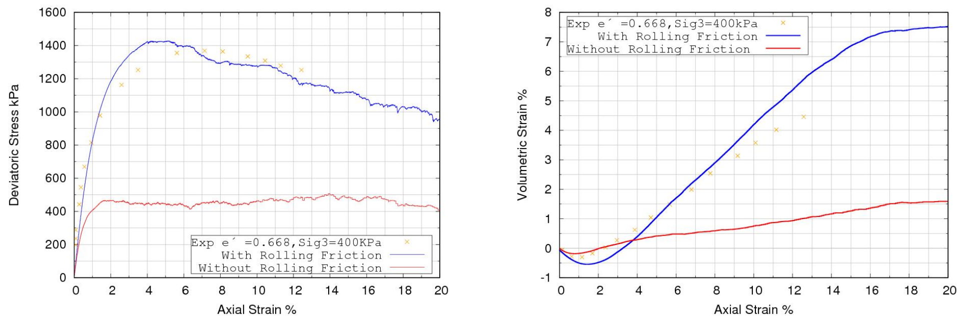

Figure 8: Effect of the rolling resistance friction on the DEM results in comparison to experimental data by Fukushima and Tatsuoka (1984). Initial void ratio=0.668 and confining pressure=400kPa

3.2. Influence of shape parameters for the polyhedral grain model

The roundness of the particle plays an important role on the mechanical response (Cho et al., 2006) so that a parametric study is carried out on the effect of the particles' roundness when using polyhedrons, through the consideration of the sweeping spheres and their rounding coefficient primarily used for the contact algorithm discussed in Section 2.1. A relative rounding coefficient for sweeping spheres of radius r_1 is defined in PFC as the ratio between r_1 and the radius r_2 of another sphere that has the same volume as the polyhedron. Fig. 9 presents three final shapes for the same initial polyhedrons P_1, P_2 and P_3 after rounding their core shapes using different relative rounding values. The simulations were performed by using the contact parameters of Set 1 (Table 5) and by using the polyhedral shapes from Group 1 (Table 1).

Table 5: 3D-DEM polyhedron model parameters

Set	Contact			Packing (see also Fig. 4 for psd)		
Number	E_{mod} (MPa)	K_n/K_s (-)	μ (-)	N_b (-)	Initial A (-)	Relative rounding (-)
Set 1	300	2	0.8	7490	-0.20	0.0001
Set 2	200	3	0.6	7490	0.26	0.0001

Fig. 10 and 11 illustrate the effect of the rounding of the particles on the macroscopic and microscopic behaviors. The initial coordination number increases by decreasing the rounding of the particles. Accordingly, the sample

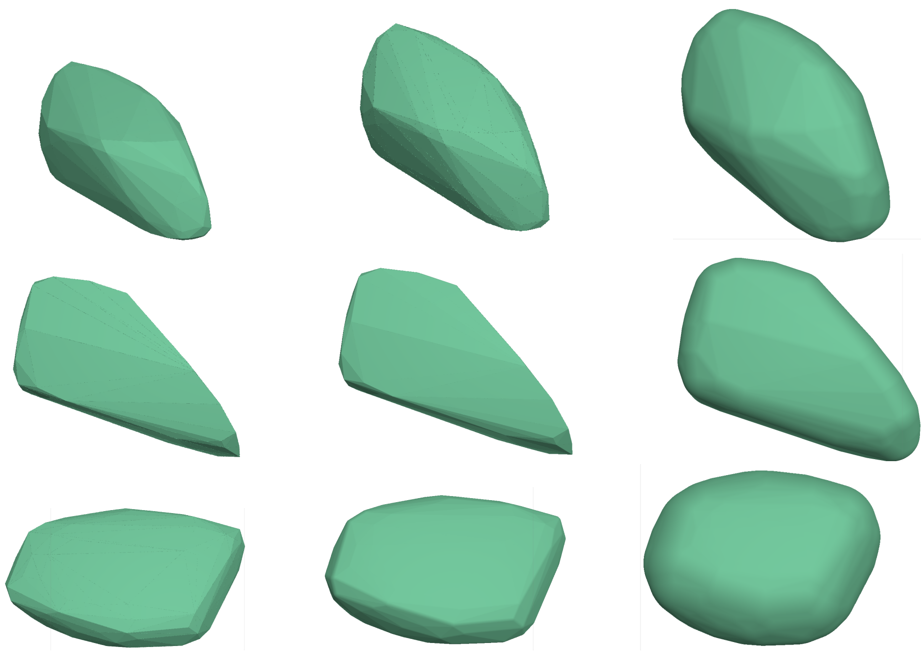

Figure 9: Different relative rounding values for particles P1 (top row), P2 (middle row) and P3 (bottom row). The particles have relative rounding values from left to right 0.0001, 0.01 and 0.5.

with a lower rounding value has a higher resistance and a larger volumetric dilation. Fig. 11 shows the evolution of the anisotropy of the contact normal fabric tensor, as per Eq. 13, during the shearing phase for various roundness values. Note that the initial anisotropy observed in the case of the polyhedron model is due to the non-spherical shapes of the polyhedron (Azéma and Radjai, 2010). The results show that the sample with a higher relative rounding value has less tendency to present an initially anisotropic fabric tensor. Finally, since Toyoura sand is observed to be the less rounded among various sands from 2D images (Liu and Yang, 2018), therefore the relative rounding value of 0.0001 is used for the calibration of the polyhedron model in Section 3.4.

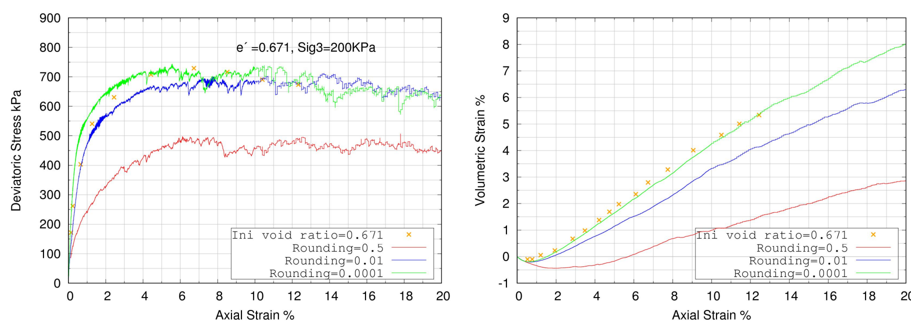

Figure 10: Evolution of deviatoric stress vs axial strain (left) and volumetric strain vs axial strain (right) for different relative rounding values. Cross points are experimental data by Fukushima and Tatsuoka (1984).

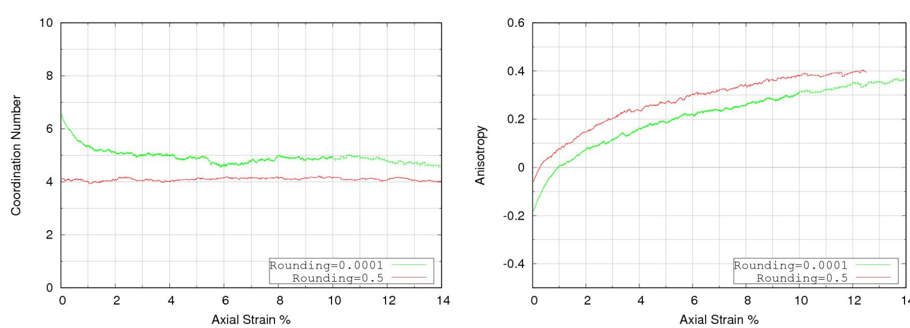

Figure 11: Evolution of the fabric tensor and coordination number vs axial strain during the drained triaxial test for different relative rounding values with a mean effective stress = 200 kPa and initial void ratio = 0.671.

Next, the effect of the particle aspect ratio is investigated by considering the Group 2 shapes with a reduced aspect ratio (Table 1) together with those of Group 1 while keeping all the other parameters constant (set 1 of Table 5). The results in Fig. 12 show the crucial role played by the particle aspect-ratio on the strength of granular material. The sample with higher aspect-ratio values, or lower values for true sphericity, has a higher resistance and a larger volumetric dilation. In addition, Fig. 13 presents the evolution of the fabric tensor and coordination number for the two groups during the triaxial compression test. The results show that the sample with particles of Group 2 (lower aspect-ratio value) has less tendency to induce an initially anisotropic fabric and lower initial coordination number.

The above results about the dependency of the initial anisotropy values on the aspect ratio and rounding values are consistent with the results of the spheres model (isotropic well-rounded particles) presented in Fig. 14 which show that the anisotropy value is almost equal to zero after the confining phase of the triaxial test.

3.3. Interplay of initial fabric with contact parameters for the polyhedron model

Unlike spheres, polyhedron packings show different initial fabric anisotropy depending on the generation procedure. Using the first method exposed in Section 2.4 (isotropic compaction), an initial anisotropy is obtained because of the irregular shapes which make the fabric more sensitive to be initially anisotropic, with $A = -0.2$ here. In the second method involving vertical settlement, packing shows an anisotropy value $A = 0.26$ which means that the contacts were more aligned vertically. It is worth mentioning that X-ray tomography of laboratory sand samples prepared by air pluviation method (Wiebicke et al., 2020) confirm the present DEM observations in two aspects. First, Wiebicke et al. (2020) observed a rounded Caicos sand to show an isotropic fabric even after pluviation, consistent with our previous observations on spheres. Second, they also measured after preparation an initially anisotropic fabric, with virtually the same A, on Hostun sand which shares similar shape features with Toyoura

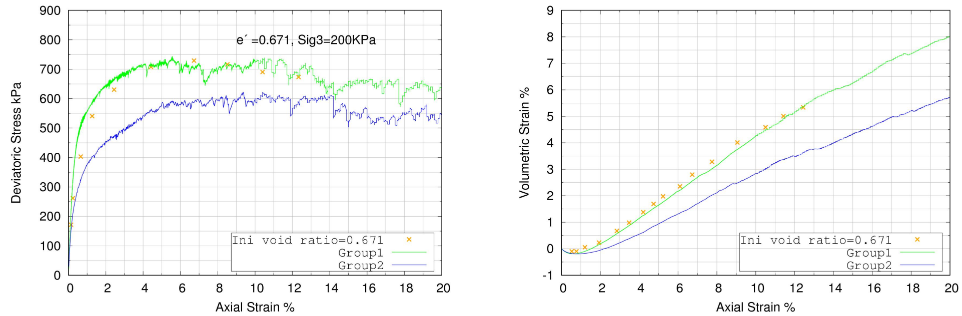

Figure 12: Evolution of deviatoric strain vs axial strain and volumetric strain vs axial strain for different aspect-ratio values. Cross points are experimental data (Fukushima and Tatsuoka, 1984).

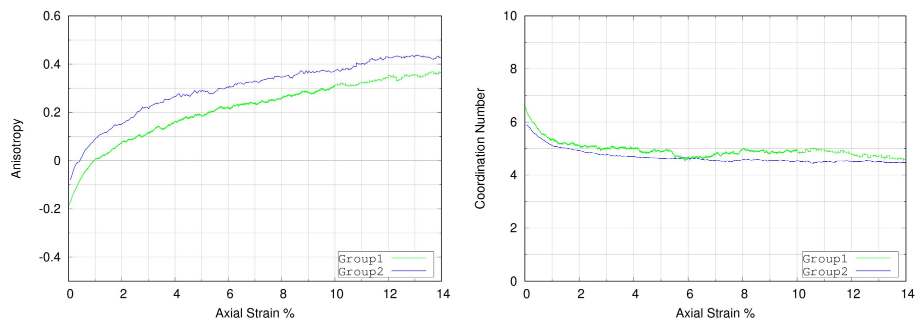

Figure 13: Evolution of the fabric tensor and coordination number vs axial strain during the drained triaxial test for different aspect-ratio values with a mean effective stress = 200 kPa and initial void ratio = 0.671.

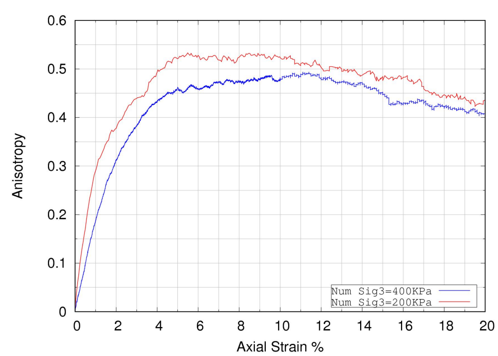

Figure 14: Evolution of the fabric anisotropy A of the sphere model during two drained triaxial tests with confining pressures = 200,400 kPa and initial void ratios = 0.671,0.668.

sand according to Altuhafi et al. (2013).

Aiming for an equivalent calibration exercise in spite of the different fabrics, both samples can still reproduce a given drained triaxial compression (Fig. 15), by using two different sets of parameters (Set 1 or 2 in Table 5). Because the Set 1 sample with initial $A = -0.2$ shows more contact normal vectors aligned to the horizontal (X, Y) plane than to the vertical direction Z which is the major principal direction for the test, it is necessary to adopt higher contact parameters in Set 1: $(E_{mod}; \mu) = (300 \text{ MPa}; 0.8)$ instead of $(200 \text{ MPa}; 0.6)$ for Set 2.

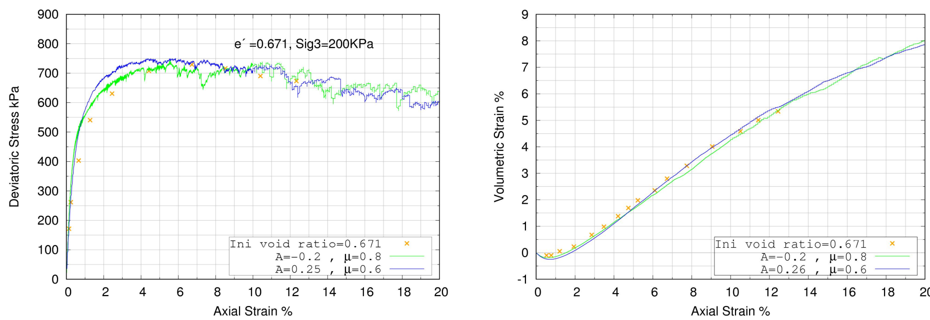

Figure 15: Two possible calibrations of the polyhedron model on a drained triaxial test by (Fukushima and Tatsuoka, 1984) by using two different sets of contact parameters in connection with two different preparation methods, i.e. fabric: Set 1 (e.g. μ=0.8 while $A = -0.2$) and Set 2 (e.g. μ=0.6 while $A = 0.26$)

The predictive performances of these two polyhedron models are then compared on different stress paths such as undrained triaxial compression and extension. Fig. 16 shows simulations of Set 1 and Set 2 for triaxial compression and extension tests at the same initial mean effective stress (400 kPa) along with experimental data of dry-deposited Toyoura sand from Yoshimine (2013). When performing such blind predictions, the model with Set 1 parameters can successfully fit the undrained triaxial compression but its behavior is much too stiff when sheared in extension. However, the model with Set 2 parameters gives a very good prediction for both the compression and extension paths in terms of deviatoric and effective mean pressure responses, as shown in Fig. 16.

These simulations highlight how DEM models may appear to show non-

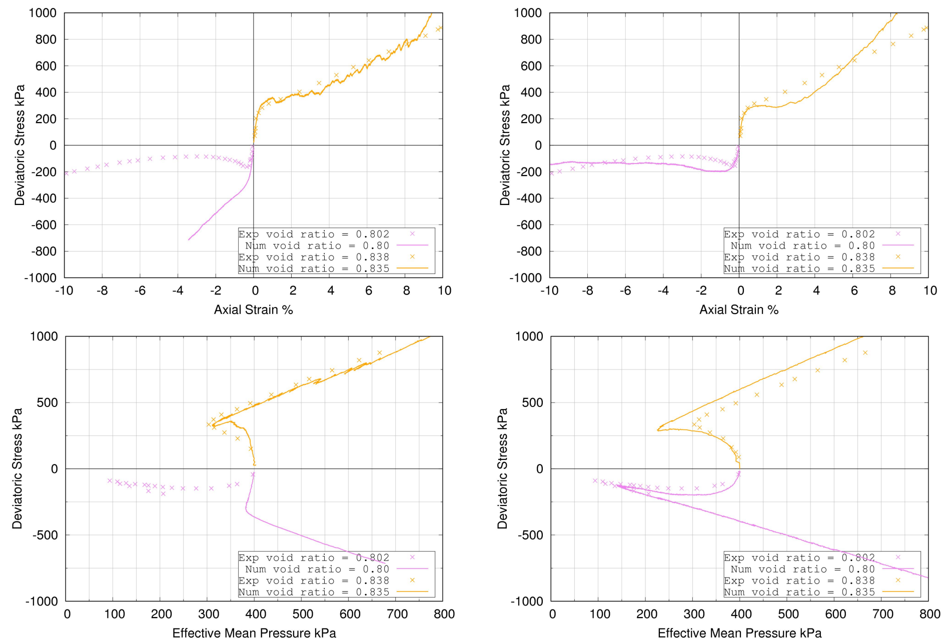

Figure 16: Predictions of two polyhedron models along undrained compression and extension stress paths against experimental data by Yoshimine (2013): interplay of packing anisotropy and contact parameters. Left: Set 1 model with A=-0.2 and e.g. μ=0.8; right: Set 2 model with A= 0.26 and e.g. μ=0.6

unique contact parameters or fail in their predictions, if one considers a limited set of loading paths or neglects fabric considerations. Here, the second preparation procedure (vertical deposition under gravity) associated with Set 2 is more similar to laboratory preparation methods (the air pluviation method) and gives a more physical fabric, with contact normal vectors that tend to align along the direction of deposition. It then enables the DEM model to be more performant along various loading paths, as it will be further evidenced in the coming sections.

3.4. Calibrated parameters

Final calibration of both spherical (with four contact parameters, Table 3) and polyhedron (with three contact parameters, Table 5) models is finally proposed, based on a drained triaxial compression test for Toyoura sand obtained by Fukushima and Tatsuoka (1984) and presented in Woo and Salgado (2015). The sphere model is calibrated for an initial void ratio and a confining pressure equal to 0.668 and 400kPa respectively, while the polyhedron model considers an initial void ratio and confining pressure equal to 0.671 and 200 kPa respectively. Other tests will be considered for validation in Section 4.1, such that both models will eventually address the same experimental data set, either in a calibration or in a validation stage. It is also recalled that the DEM models have initial void ratio values equal to the experimental void ratios for the different triaxial tests, see Section 2.4.

Following Sections 3.2 3.3, the polyhedron model adopts particles with Group 1 shapes and the Set 2 configuration in Table 5 because laboratory samples were prepared using the air pluviation method.

The calibration results of both models can closely fit the experimental data as shown in Fig. 17. It is remarkable that the friction coefficient is the same in both DEM approaches, highlighting the role of the rolling resistance model to take into account complex particle shapes in an indirect way.

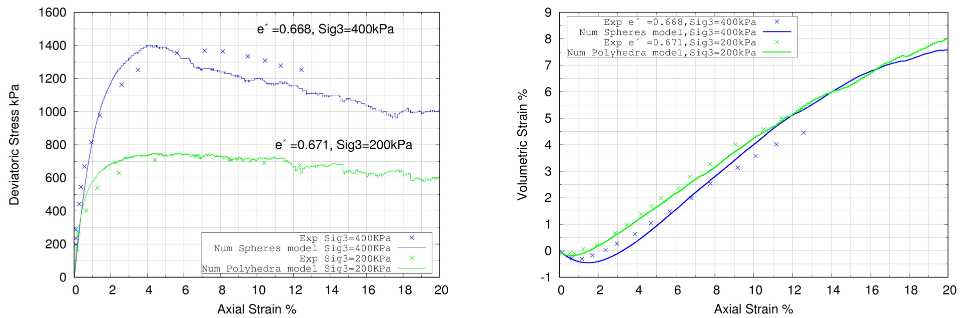

Figure 17: Calibration of the sphere and polyhedron models by using one drained triaxial test in each case. The cross points are experimental data (Fukushima and Tatsuoka, 1984).

4. Validation of the sphere and polyhedron models and discussion

4.1. Validation

The two models were finally validated checking their prediction abilities for other drained triaxial tests and for undrained conditions.

Fig. 18 and 19 represent the predictions of sphere and polyhedron models together with the experimental results for the drained triaxial tests for various initial void ratios and confining pressures. The results of the two models present a good fit with the corresponding experimental results for the deviatoric stress and volumetric strain responses. A slight difference is just to note for the volumetric strain behavior in the case of the two relatively loose (less dilatant) samples. We observed in other simulations with spheres, not presented here, that introducing a flexible membrane boundary condition instead of rigid walls would slightly improve the agreement for these two tests.

As for the undrained compression tests, a fully strain-controlled model with constant volume is used to simulate such a loading condition. Simulations are reported for extension and compression conditions and for six samples with different initial void ratio values which ranged between 0.794 and 0.88 and could be obtained systematically in the simulations. The simulated responses agree closely with the experimental data, revealing the good capability of the proposed models to capture the complex behavior of the granular material during the undrained conditions, as shown in Fig. 20 and 21. Firstly, the behavior

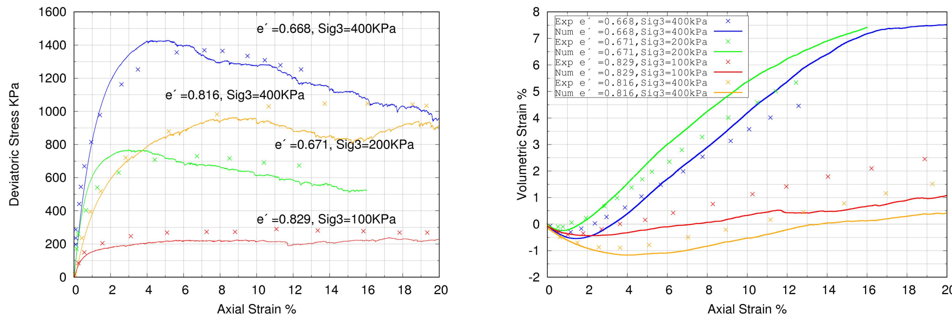

Figure 18: Behavior of the sphere model for Toyoura sand under various drained triaxial compressions serving as calibration ($e_0 = 0.668; \sigma_3 = 400$ kPa) and validation paths. Experimental data from (Fukushima and Tatsuoka, 1984)

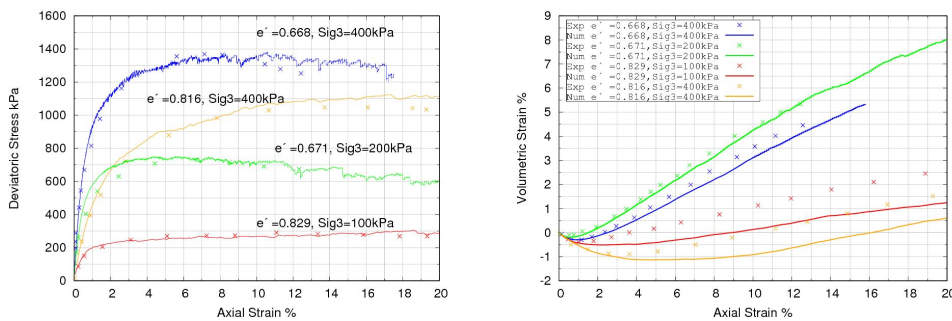

Figure 19: Behavior of the polyhedron model for Toyoura sand along various drained triaxial compressions serving as calibration ($e_0 = 0.671; \sigma_3 = 200$ kPa) and validation paths. Experimental data from (Fukushima and Tatsuoka, 1984)

is sensitive to different initial void ratios. Secondly, the model captures the difference between the extension and compression triaxial behaviors naturally, confirming the fact that the sand response is much more contractive in triaxial extension than when loaded in triaxial compression.

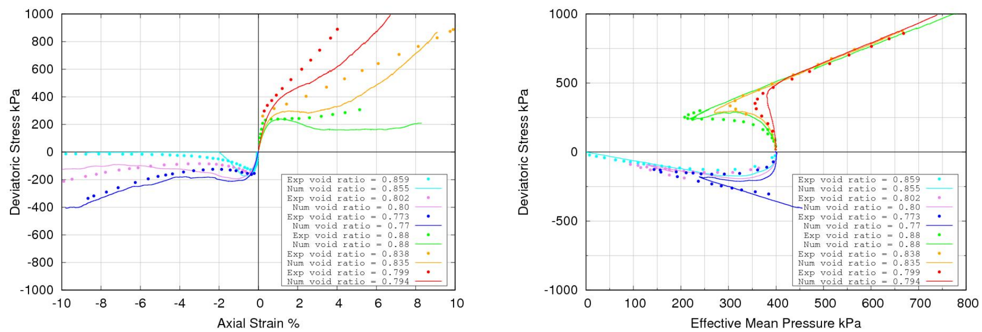

Figure 20: Validation of sphere model for Toyoura sand sheared under undrained triaxial extension and compression for various void ratios and an initial mean effective pressure = 400 kPa. Experimental data by (Yoshimine, 2013).

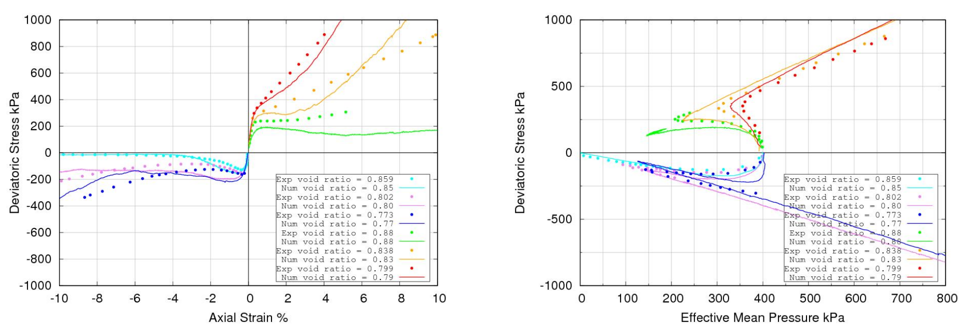

Figure 21: Validation of the polyhedral grain model for Toyoura sand under undrained triaxial extension and compression for various void ratios and an initial mean effective pressure = 400 kPa. Experimental data by (Yoshimine, 2013).

4.2. Discussion

While the two models give very good predictions for the macroscopic mechanical behavior of Toyoura sand, the polyhedron model showed a somewhat higher capability of fitting the volumetric strain behavior and especially the initial contraction regime and substantial differences remain from a microscopic point of view. For example, for the same initial void ratios, the 3D-DEM polyhedron model has an initial coordination number higher than the 3D-DEM model with the rolling resistance model, as shown in Fig. 22.

Furthermore, since the polyhedral model contained flat and angular-shaped particles, the sample showed an inherent anisotropy, which is a function of the generation procedure. This feature was reported in previous studies of Toyoura sand (Yoshimine et al., 1998; Tatsuoka et al., 1986) and could not be captured by using spherical particles. While this has not been detrimental to the performances of the spherical model in the present study on monotonous paths, some unrealistic fabric for spheres model has been reported by Zhao et al. (2018), which may relate with lower predictions abilities of these approaches in some cases, such as cyclic undrained triaxial test (Gu et al., 2020; Sibille et al., 2021).

On practical aspects, the simulations using the polyhedral particles are still a time-consuming task, with the calculation time depending on the number of vertices of each piece utilized inside the contact detection scheme. Fig. 22 shows that the computational time of the present 3D-DEM polyhedron model was almost 9 times higher than the 3D-DEM model with a rolling resistance model and for the same numerical conditions. However, the rolling resistance contact model includes four contact mechanical parameters which are somewhat tedious to calibrate, while only three such parameters are required for the polyhedron model. While some complexity hides in the latter model behind the characterization of the representative shapes, experimental techniques are getting more and more available for a direct measurement of those shapes (e.g. Katagiri et al., 2010; Rorato et al., 2021).

5. Conclusions

This paper has established two discrete element models with different kinds of rigid particles for describing the microscopic and macroscopic behaviors of Toyoura sand, as well as a thorough study on important model features from the particle- to the packing-scale.

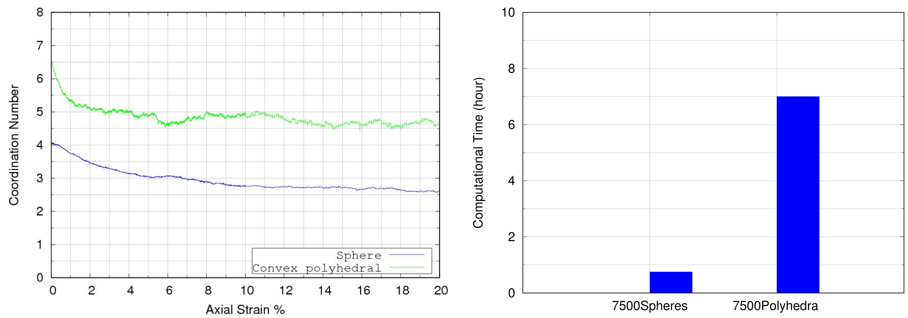

Figure 22: Left: evolution of the coordination number for the sphere model and convex polyhedron model during drained triaxial test with an initial porosity n=0.402. Right: computation time for two drained triaxial tests for the two models with a target axial strain = 0.2.

At the particle scale, the crucial role of shapes, roughnesses and angularity of Toyoura sand grains on its mechanical response was taken into account within the 3D-DEM simulations, either artificially by adding rolling resistance stiffness between spherical particles or by introducing the realistic particles via convex polyhedron shapes. The convex polyhedron model was an image-based model in which the 2D shape and the aspect-ratio of three different real particles of Toyoura sand were used to create three representative particles for Toyoura sand that shared the same number of particles inside the 3D-DEM model. For a better control over the shapes proposed, a parametric study was carried out on the effect of the particles' roundness and aspect ratio on the mechanical response. The results first showed that samples with a lower aspect ratio and a higher roundness value have less tendency to be initially anisotropic after an isotropic packing preparation. Second, the strength of the sample increased with an increasing particle aspect ratio and a decreasing roundness, along with a more dilatant volumetric response.

At the packing-scale, the REV configuration in terms of the number of particles is the first important issue. As for the optimization of a 3D-DEM simulation, 7500 particles were chosen to construct a homogeneous sample in terms of porosity, showing a unique stress-strain behavior. Moreover, a study on the effect of the initial fabric on triaxial compression and extension tests emphasized once more the crucial role played by the initial contact normal orientation on the mechanical response. This parameter corresponded to different sample preparation methods for the laboratory triaxial tests. Having a sample that was prepared in the same way as the experimental laboratory sample, allowed us to select one set of parameters capable of calibrating and validating different stress paths. The numerical simulations of the two models of Toyoura sand proposed showed remarkable quantitative and qualitative agreement with the experimental results for various stress paths and a wide range of initial void ratios.

Finally, the computational time for the convex polyhedron model was found to be nine times higher than that of the sphere model using the same numerical conditions such as the number of particles, strain rate and final axial strain value.

Acknowledgements

This work was supported by the Suez Consulting company (P. Soulat). Furthermore, the authors would like to express their sincere thanks and gratitude to the Itasca Educational Partnership Program (IEP, S. Emam) for their valuable support and for providing PFC software.

References

Ai, J., Chen, J.F., Rotter, J.M., Ooi, J.Y., 2011. Assessment of rolling resistance models in discrete element simulations. Powder Technology 206, 269–282.

Altuhafi, F., O'Sullivan, C., Cavarretta, I., 2013. Analysis of an image-based method to quantify the size and shape of sand particles. Journal of Geotechnical and Geoenvironmental Engineering 139, 1290–1307. doi:10.1061/(ASCE)GT.1943-5606.0000855.

Azéma, E., Radjai, F., 2010. Stress-strain behavior and geometrical properties of packings of elongated particles. Physical Review E 81, 051304.

Bergen, G.v.d., 1999. A fast and robust GJK implementation for collision detection of convex objects. Journal of graphics tools 4, 7–25.

Chareyre, B., 2003. Modélisation du comportement d'ouvrages composites sol-géosynthétique par éléments discrets: application aux ancrages en tranchées en tête de talus. Ph.D. thesis. Université Joseph-fourier-Grenoble I.

Cheng, H., Shuku, T., Thoeni, K., Yamamoto, H., 2018. Probabilistic calibration of discrete element simulations using the sequential quasi-monte carlo filter. Granular matter 20, 1–19.

Cho, G.C., Dodds, J., Santamarina, J.C., 2006. Particle shape effects on packing density, stiffness, and strength: Natural and crushed sands. Journal of Geotechnical and Geoenvironmental Engineering 132, 591–602. doi:10.1061/(ASCE)1090-0241(2006)132:5(591).

Cundall, P.A., Strack, O.D., 1979. A discrete numerical model for granular assemblies. Geotechnique 29, 47–65.

Dong, Q., Xu, C., Cai, Y., Juang, H., Wang, J., Yang, Z., Gu, C., 2016. Drained instability in loose granular material. International Journal of Geomechanics 16, 04015043.

Duriez, J., Bonelli, S., 2021. Precision and computational costs of Level Set-Discrete Element Method (LS-DEM) with respect to DEM. Computers and Geotechnics 134, 104033. doi:10.1016/j.compgeo.2021.104033.

Duverger, S., Duriez, J., Philippe, P., Bonelli, S., 2021. Rattlers´ involvement for possibly looser critical states under higher mean stress. EPJ Web Conf. 249, 11002. doi:10.1051/epjconf/202124911002. proc. of Powders & Grains 2021.

Fukushima, S., Tatsuoka, F., 1984. Strength and deformation characteristics of saturated sand at extremely low pressures. Soils and Foundations 24, 30–48.

Garcia, X., Latham, J.P., Xiang, J.S., Harrison, J., 2009. A clustered overlapping sphere algorithm to represent real particles in discrete element modelling. Geotechnique 59, 779–784.

Gilbert, E., Johnson, D., Keerthi, S., 1988. A fast procedure for computing the distance between complex objects in three-dimensional space. IEEE Journal on Robotics and Automation 4, 193–203. doi:10.1109/56.2083.

Gu, X., Zhang, J., Huang, X., 2020. Dem analysis of monotonic and cyclic behaviors of sand based on critical state soil mechanics framework. Computers and Geotechnics 128, 103787.

Hosn, R.A., Sibille, L., Benahmed, N., Chareyre, B., 2017. Discrete numerical modeling of loose soil with spherical particles and interparticle rolling friction. Granular matter 19, 4.

Irazábal, J., Salazar, F., Oñate, E., 2017. Numerical modelling of granular materials with spherical discrete particles and the bounded rolling friction model. application to railway ballast. Computers and Geotechnics 85, 220–229.

Itasca, 2018. Pfc — particle flow code, ver. 6.0. Itasca Consulting Group, Inc.

Iwashita, K., Oda, M., 1998. Rolling resistance at contacts in simulation of shear band development by dem. Journal of engineering mechanics 124, 285–292.

Jerves, A.X., Kawamoto, R.Y., Andrade, J.E., 2016. Effects of grain morphology on critical state: a computational analysis. Acta Geotechnica 11, 493–503. doi:10.1007/s11440-015-0422-8.

Jiang, M., Shen, Z., Wang, J., 2015. A novel three-dimensional contact model for granulates incorporating rolling and twisting resistances. Computers and Geotechnics 65, 147–163.

Katagiri, J., Matsushima, T., Yamada, Y., 2010. Simple shear simulation of 3d irregularly-shaped particles by image-based dem. Granular Matter 12, 491–497.

Lee, S.J., Hashash, Y.M., Nezami, E.G., 2012. Simulation of triaxial compression tests with polyhedral discrete elements. Computers and Geotechnics 43, 92–100.

Li, B., 2011. Effect of fabric anisotropy on the dynamic mechanical behavior of granular materials. Ph.D. thesis. Case Western Reserve University.

Li, X.S., Dafalias, Y.F., 2012. Anisotropic critical state theory: Role of fabric. Journal of Engineering Mechanics 138, 263–275. doi:10.1061/(ASCE)EM.1943-7889.0000324.

Liu, X., Yang, J., 2018. Shear wave velocity in sand: effect of grain shape. Géotechnique 68, 742–748.

Miura, K., Maeda, K., Furukawa, M., Toki, S., 1998. Mechanical characteristics of sands with different primary properties. Soils and Foundations 38, 159–172.

Nassauer, B., Liedke, T., Kuna, M., 2013. Polyhedral particles for the discrete element method. Granular matter 15, 85–93.

Nguyen, T.K., Combe, G., Caillerie, D., Desrues, J., 2014. Fem× dem modelling of cohesive granular materials: numerical homogenisation and multi-scale simulations. Acta Geophysica 62, 1109–1126.

Oda, M., Nemat-Nasser, S., Konishi, J., 1985. Stress-induced anisotropy in granular masses. Soils and Foundations 25, 85–97.

Preparata, F.P., Muller, D.E., 1979. Finding the intersection of n half-spaces in time o (n log n). Theoretical Computer Science 8, 45–55.

Rorato, R., Arroyo, M., Gens, A., Andò, E., Viggiani, G., 2021. Image-based calibration of rolling resistance in discrete element models of sand. Computers and Geotechnics 131, 103929.

Shamos, M.I., Hoey, D., 1976. Geometric intersection problems, in: 17th Annual Symposium on Foundations of Computer Science (sfcs 1976), IEEE. pp. 208–215.

Shinohara, K., Oida, M., Golman, B., 2000. Effect of particle shape on angle of internal friction by triaxial compression test. Powder technology 107, 131–136.

Sibille, L., Benahmed, N., Darve, F., 2021. Constitutive response predictions of both dense and loose soils with a discrete element model. Computers and Geotechnics 135, 104161.

Sibille, L., Villard, P., Darve, F., Aboul Hosn, R., 2019. Quantitative prediction of discrete element models on complex loading paths. International Journal for Numerical and Analytical Methods in Geomechanics 43, 858–887.

Tatsuoka, F., Sakamoto, M., Kawamura, T., Fukushima, S., 1986. Strength and deformation characteristics of sand in plane strain compression at extremely low pressures. Soils and Foundations 26, 65–84.

Verdugo, R., Ishihara, K., 1996. The steady state of sandy soils. Soils and foundations 36, 81–91.

Wadell, H., 1932. Volume, shape, and roundness of rock particles. The Journal of Geology 40, 443–451. doi:10.1086/623964.

Wang, R., Fu, P., Zhang, J.M., Dafalias, Y.F., 2016. Dem study of fabric features governing undrained post-liquefaction shear deformation of sand. Acta Geotechnica 11, 1321–1337.

Wiebicke, M., Andò, E., Viggiani, G., Herle, I., 2020. Measuring the evolution of contact fabric in shear bands with x-ray tomography. Acta Geotechnica 15, 79–93.

Woo, S.I., Salgado, R., 2015. Bounding surface modeling of sand with consideration of fabric and its evolution during monotonic shearing. International Journal of Solids and Structures 63, 277–288.

Yimsiri, S., Soga, K., 2010. DEM analysis of soil fabric effects on behaviour of sand. Géotechnique 60, 483–495.

Yokura, K., Yamamoto, H., Wu, Y., 2015. Crushing tests of soil particles by high pressure true tri-axial compression apparatus. Japanese Geotechnical Society Special Publication 1, 51–56.

Yoshimine, M., 2013. Yoshimine m. archives – soil mechanics laboratory. Tokyo Metro-politan.

Yoshimine, M., Ishihara, K., Vargas, W., 1998. Effects of principal stress direction and intermediate principal stress on undrained shear behavior of sand. Soils and Foundations 38, 179–188.

Zhao, S., Evans, T.M., Zhou, X., 2018. Shear-induced anisotropy of granular materials with rolling resistance and particle shape effects. International Journal of Solids and Structures 150, 268–281.

Zhao, S., Zhao, J., 2021. Sudodem: Unleashing the predictive power of the discrete element method on simulation for non-spherical granular particles. Computer Physics Communications 259, 107670.